https://doi.org/10.5194/egusphere-2025-1568
Preprint. Discussion started: 30 July 2025

Towards better black carbon emission estimates in Europe: assimilating observations with a Bayesian inversion framework

August Thomasson[1], Pontus Roldin[1], Nick Schutgens[2], Babitha George[2], Hugo Denier van der Gon[3], Guillaume Monteil[4], and Marko Scholze[5]

[1]Department of Physics, Lund University, Lund, 223 62, Sweden
[2]Faculty of Science, Vrije Universiteit Amsterdam, 1081 HV Amsterdam
[3]Department of Air Quality and Emissions Research, TNO, Utrecht, The Netherlands
[4]Barcelona Supercomputing Center, Barcelona, Spain
[5]Department of Physical Geography and Ecosystem Science, Lund University, Lund, 223 62, Sweden

Correspondence: August Thomasson (august.thomasson@fysik.lu.se)

Abstract. There are large discrepancies between different black carbon (BC) bottom-up emission estimates. This affects our understanding of how BC affects population health and climate. Previous studies have presented top-down estimates in various domains but estimates in Europe for more than a few months are lacking. With the Lund University Modular Inversion Algorithm (LUMIA) and the FLEXible PARTicle dispersion model (FLEXPART), we aim to calculate top-down estimates of anthropogenic BC emissions by assimilating surface observations from 24 background sites in Europe (15° W—35° E, 33–73° N) during 2021. The results show that the bottom-up BC inventory generally underestimates emissions in the domain. Annually, the resulting top-down emissions are 411 ± 10 Gg of BC, 18% higher than the bottom-up estimate of 349 ± 30 Gg used as a prior. The largest increases in emissions occur in Eastern parts of Europe during spring and summer, while emissions in Poland and Italy are reduced during winter and autumn. The overall posterior emissions are most sensitive to changes in the observational network on the periphery, resulting in a reduced standard deviation compared to the prior emissions in the central domain, where the network density is high. A cross-validation scheme, where one site at the time is removed for validation, show that the posterior for a majority of sites fit independent observations better than the prior emissions.

1 Introduction

Black carbon (BC) is a component of atmospheric particles originating mainly from incomplete combustion of carbonaceous fuels. BC negatively affects air quality and public health as a component of fine particulate matter ($PM_{2.5}$) and due to its ability to carry a wide variety of possible toxic chemicals to the lungs (Janssen et al., 2012). In addition, BC is a driver of climate change since it has light-absorbing properties. BC's global effective radiative forcing is around 0.15 ± 0.17 W m^{-2} (Thornhill et al., 2021), but due to its short lifetime, it can have larger effects on smaller spatio-temporal scales (Hodnebrog et al., 2014).

https://doi.org/10.5194/egusphere-2025-1568
Preprint. Discussion started: 30 July 2025

BC is also involved in snow—albedo feedbacks, as particles deposited on snow can drastically decrease the albedo (Clarke and Noone, 1985). At the same time, there are large uncertainties surrounding our understanding of how atmospheric BC concentration affects population health and climate. Uncertainties in emission estimates contribute to the overall uncertainty of modelled BC concentrations. Therefore, more robust BC emission quantification is crucial.

Traditionally, emissions of BC, and other atmospheric species in general, are estimated with a direct, *bottom-up* approach. These are based on emission factors, activity data, and other proxy information. While they provide important knowledge about the spatio-temporal distribution of BC emissions, these proxy data sources are often coarsely modelled, interpolated from a few data points or derived from idealized laboratory experiments and short field campaigns (Cohen and Wang, 2014). In addition, important sources, specifically flaring, of BC have been shown to be missing in bottom-up inventories (Stohl et al., 2013). The significant uncertainty in emissions partly explains why there are large differences between observed and modelled BC concentrations based on bottom-up inventories (Koch et al., 2009), as well as why there are large discrepancies between different bottom-up inventories.

In light of this, different *top-down* approaches, i.e. inverse methods, can be utilized as a complement to bottom-up inventories. The top-down approach infers changes to the emission inventories based on atmospheric observations of BC, often surface concentrations. While this approach can reduce uncertainties in the emissions estimates as compared to the bottom-up inventories, other limitations are introduced. For example, inversion systems are generally computationally heavy, and their accuracy is dependent on the density of available observations, limiting the spatio-temporal resolution and domain they can be utilized on. Therefore, previous top-down BC emissions estimates have relatively coarse resolution, spatially and/or temporally. Cohen and Wang (2014) used a Kalman filter to estimate monthly global BC emissions on nine regions based on surface observations and satellite retrievals. Zhang et al. (2015) used satellite derived Aerosol Optical Depth and a variational inversion approach to constrain BC emissions in Asia, spatially (0.5° x 0.667°) resolved for two months. In China, BC emissions have been evaluated with multiple top-down approaches using surface observations, for example with multilinear regression for five regions (Wang et al., 2013), monthly city cluster emissions (Zhao et al., 2019) and an ensemble optimal interpolation on a 0.5° grid and monthly temporal scale (Wang et al., 2016). In the USA, Mao et al. (2014) produced top-down emissions of BC in 5 regions and sectors with an analytical solution to the inverse problem based on surface observations. Guerrette and Henze (2017) used a 4D variational approach with surface and airborne observations to solve for daily BC emissions for a three-day case study on an irregular grid. Utilizing the same transport model as the present study (see Sect. 2.1), Evangeliou et al. (2018) used surface observations to optimize monthly BC emissions for three years in the Arctic with a Bayesian inversion approach. The emissions are optimized monthly on an irregular grid between 8° and 1°. The same inversion system was later used to investigate BC emissions during COVID-19 lockdown in Europe (Evangeliou et al., 2021) and China (Jia et al., 2021), with a similar irregular grid on a weekly basis limited to January—April from 2015—2020. In addition, recent development in assimilation of satellite observation of aerosol (absorption) optical depth show a global underestimation in BC emissions (Chen et al., 2022; Tsikerdekis et al., 2023).

With recent developments in inverse modelling techniques, increasing amount of computational power, as well as an increasing number of BC monitoring sites, there is an opportunity for top-down BC emissions to be constrained on finer scales

https://doi.org/10.5194/egusphere-2025-1568
Preprint. Discussion started: 30 July 2025

than previously. In this study, we present the first application of the Lund University Modular Inversion Algorithm (LUMIA, described in Sect. 2) (Monteil and Scholze, 2021) to top-down emission estimates of black carbon, in Europe (15° W–35° E, 33–73° N) specifically. By leveraging the offline transport in LUMIA, reducing computational constraints at the cost of memory storage, it is possible to compute the inversion with the daily BC emissions on a 0.25° x 0.25° grid; a finer spatio-temporal scale than previous top-down BC emission estimates. This allows for a better understanding of the variability in emissions within Europe, and within individual European countries. The present study focuses on 2021. As this is the first application of LUMIA to top-down emission estimates of aerosols, the main aim of this study is to test and validate the system. We test the setup with several synthetic experiments and sensitivity tests, and validate it using a cross-validation scheme. The paper is organized as follows: first, we present the inversion framework (Sect. 2) followed by a description of the input data (Sect. 3) which includes prior emissions (3.1) and the observational network (3.2). Then, the different inversion setups and experiments are described in detail (Sect. 4), followed by the results from the synthetic and real inversions (Sect. 5). Finally, the results are discussed (Sect. 6) and some final conclusions are presented (Sect. 7).

2 Inversion framework

The inversions are performed with the Lund University Modular Inversion Algorithm (LUMIA). LUMIA is described in detailed in Monteil and Scholze (2021) where it is applied to regional CO_2 inversions. The framework uses a Bayesian variational algorithm to solve the inversion problem (Meirink et al., 2008). The aim is to find the most probable set of emissions given a set of prior emissions and atmospheric observations considering the uncertainties in both. The emissions (in the control space called the control vector $\boldsymbol{x}$, where each element is the anthropogenic BC emissions at a given grid point and day) are related to the observations (the observation vector $\boldsymbol{y}$) with a numerical model of atmospheric transport H.

$$\boldsymbol{y} = H(\boldsymbol{x}) + \epsilon \tag{1}$$

Since the transport model (see Sect. 2.1) is linear, $H(\boldsymbol{x})$ simplifies to $\mathbf{H}\boldsymbol{x}$ where $\mathbf{H}$ is the Jacobian of the transport model. This is advantageous since the Jacobian matrix can be precomputed. The error term, ϵ, includes both model representation, spatio-temporal representation and observational errors. Finding the most probable emissions is mathematically equivalent to finding the control vector $\hat{\boldsymbol{x}}$ that minimizes the cost function $\boldsymbol{J}(\boldsymbol{x})$.

$$\boldsymbol{J}(\boldsymbol{x}) = \frac{1}{2}(\boldsymbol{x} - \boldsymbol{x_b})^T \mathbf{B}^{-1}(\boldsymbol{x} - \boldsymbol{x_b}) + \frac{1}{2}(\boldsymbol{y} - \mathbf{H}\boldsymbol{x})^T \mathbf{R}^{-1}(\boldsymbol{y} - \mathbf{H}\boldsymbol{x}) \tag{2}$$

The first term of cost function weights the deviation of the control vector from the prior ($\boldsymbol{x_b}$) with the prior error covariance matrix ($\mathbf{B}$). The second term weights the deviation of the modelled concentrations from observations with the observation and model representation error covariance matrix ($\mathbf{R}$). Thus, minimizing $\boldsymbol{J}(\boldsymbol{x})$ provides a statistical compromise between prior emissions and observations considering their uncertainty.

With the Bayesian variational inversion algorithm, LUMIA minimizes the cost function with an iterative gradient-descent technique (see Monteil and Scholze (2021) for details). It should be noted that for efficiency reasons, the optimization occurs

https://doi.org/10.5194/egusphere-2025-1568
Preprint. Discussion started: 30 July 2025

on a preconditioned control vector $\boldsymbol{\omega} = \mathbf{B}^{1/2}(\boldsymbol{x} - \boldsymbol{x_b})$ which encodes the effects of the error covariance matrix into the control vector. This is utilized in the ensemble method described in more detail in section 4.1.

In each minimization iteration both the local cost function $\boldsymbol{J}(\boldsymbol{x})$ and its gradient $\nabla_x \boldsymbol{J}(\boldsymbol{x})$ are computed. This requires both the forward, $\mathbf{H}$, and adjoint, $\mathbf{H^T}$, of the transport, which would be computationally expensive if the transport model was executed each iteration. Instead, LUMIA employs an offline transport module based on precomputed footprints. This greatly reduces computational cost by significantly increasing storage. Section 2.1 describes how the footprints are calculated.

2.1 Transport model

The FLEXible PARTicle (FLEXPART) dispersion model version 10.4 (Pisso et al., 2019) is used to model the transport of BC in the atmosphere. FLEXPART is a Lagrangian model that has several benefits over Eulerian counterparts, namely that it is not subject to numerical diffusion and is not limited to a grid resolution, useful when calculating how sensitive an observational site is to emissions in any given location. How sensitive a site is to emissions in a grid in the model layer closest to the surface is often called a footprint.

In FLEXPART, dispersion backwards in time is simulated by releasing numerous virtual particles for a given location in space and time. The corresponding footprint for that location is calculated by aggregating the residence time of each virtual particle in each space-time grid box defined by the inversion grid (Seibert and Frank, 2004) and an arbitrary altitude threshold of 100 m (Pisso et al., 2019; Munassar et al., 2023). Calculating footprints backwards in time is numerically more efficient in our case, since we have fewer observational sites than grid cells. It also has the benefit of being able to initiate the simulations at the exact location of the site, without representation errors from a grid.

The simulations were driven by meteorological data from the European Center for Medium Range Weather Forecast (ECMWF) reanalysis product ERA5 (Hersbach et al., 2020). The data were extracted on the same domain and resolution as the inversion grid, i.e. hourly values on 0.25° grid (Pisso et al., 2019).

FLEXPART simulates both dry and wet deposition. For dry deposition, all tracers were initiated from a log-normal size distribution with mean diameter of 0.25 µm and a normalized standard deviation of 3.3, as well as a density of 1500 kg m^{-3} (Long et al., 2013). For wet deposition, different parameters can be used to control the efficiency of scavenging and deposition. We used the standard settings for BC, following the findings of Evangeliou et al. (2018). Rain and snow collection efficiency of 1 for below cloud scavenging and for in-cloud scavenging, a cloud condensation nuclei efficiency of 0.9 and ice nuclei efficiency of 0.1.

For each observation, a 24-hour footprint 14 days backwards in time was calculated (shorter if the particles exit the domain). This should be sufficient time to ensure that the model captures all contributions to the BC concentration at most observations given that there are major BC sources within the domain and that the lifetime of BC is between 4—10 days in the atmosphere (Park et al., 2005; Textor et al., 2006). However, in some cases, the air mass leaves the domain within the lifetime of BC therefore we also compute background concentrations.

https://doi.org/10.5194/egusphere-2025-1568
Preprint. Discussion started: 30 July 2025

2.2 Background concentrations

Background concentrations for each observation are calculated using the LUMIA forward operator on a larger domain (entire Northern Hemisphere, we assume the Southern Hemisphere has no impact) with lower resolution (0.5°x0.5°). This transport is driven by 30 days FLEXPART simulations and we used the CAMS-GLOBv5.3 monthly emissions (presented in Table1) and the GFEDv4s product (van der Werf et al., 2017) for wildfires.

The background concentrations, y^{bg} are calculated with Eq. 3,

$$y^{bg} = y_{NH} - y_{NH}^{fg} \tag{3}$$

where y_{NH} is the concentration given emissions in the entire NH. The foreground concentrations, y_{NH}^{fg}, are only from contributions within the regional domain, i.e. with emissions set to zero everywhere except in the inversion domain. The main benefit of this method is that the effect the regional emissions can have on the boundary condition is preserved. In other words, cases where the air mass leaves the domain but then returns are considered. In addition, it should be mentioned that the total emissions are not relevant for the background calculations; rather the relationship between the in- and outside-domain emissions is. Here, we assume this relation to be represented well enough in CAMS.

3 Input data

3.1 Prior emissions

The present study utilizes several bottom-up emission inventories for the different experiments. They are summarized in Table 1. The main dataset that is optimized in the real inversion is a modified version of HTAPv3 emission dataset (Crippa et al., 2023). HTAPv3 is a so-called mosaic dataset where more accurate regional emission inventories are merged in the global EDGAR emission dataset. The details of the modifications are presented in Denier van der Gon et al. (2023). In short, the modifications are twofold: the European data have been extrapolated from the final year of HTAPv3, 2018, to the study year of 2021 based on the CAMS-REGv5 (Kuenen et al., 2022) changes between these two years, and they include the contribution from the condensable PM fraction for residential wood/coal combustion in a consistent way following the approach outlined in Denier van der Gon et al. (2015). In addition, we apply weekly emission profiles from Guevara et al. (2021) for aviation, energy, industry and road transport sectors. Furthermore, residential heating is scaled with daily emission factors based on the concept of heating-degree-day factors, where the emissions are scaled based on ERA5 2-meter temperature (Guevara et al., 2021).

The CAMS-GLOB-ANT-v5.3 is used both to calculate background concentrations (see Sect. 2.2), and as a prior in the synthetic experiment (Sect. 4). For wildfire BC emissions, both in and outside the domain, we use the GFEDv4s product (van der Werf et al., 2017) on a daily resolution, excluding the agricultural waste burning sector, as it is already included in the anthropogenic emissions. As seen in Table 1, the magnitude of the European wildfire emissions is around two orders of magnitude lower than the anthropogenic sources.

https://doi.org/10.5194/egusphere-2025-1568
Preprint. Discussion started: 30 July 2025

Table 1. List of prior emission datasets used in the study.

Category	Product	Resolution	Domain	Provider/reference	Usage	Total emissions 2021
Anthropogenic	HTAPv3, modified	0.25°x 0.25°, daily	Europe	Crippa et al. (2023); Denier van der Gon et al. (2023)	Real; prior & Synthetic; truth	352 Gg
Anthropogenic	CAMS-GLOB-ANT-v5.3	0.25°x 0.25°, monthly	Europe	Soulie et al. (2024)	Synthetic; prior	227 Gg
Wildfires, excl. waste burning	GFEDv4s	0.25°x 0.25°, daily	Europe	van der Werf et al. (2017)	Real; prior	5 Gg
Anthropogenic	CAMS-GLOB-ANT-v5.3	0.5°x 0.5°, monthly	Northern Hemisphere	Soulie et al. (2024)	Real; background	4785 Gg
Wildfires, excl. waste burning	GFEDv4s	0.5°x 0.5°, daily	Northern Hemisphere	van der Werf et al. (2017)	Real; background	973 Gg

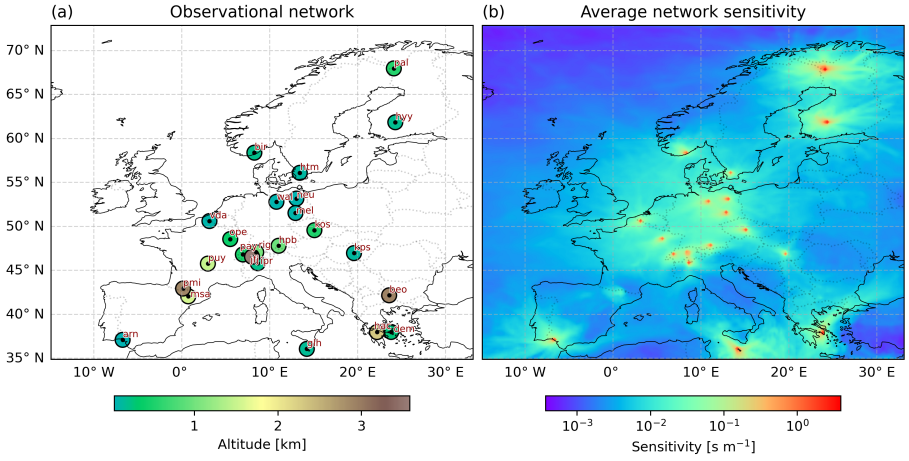

Figure 1. The network of observational sites used for the inversion (**a**), where the color shows the site's altitude. Sensitivity of the observations to emissions in the lower atmosphere, averaged over all sites and for the entire year (**b**).

3.1.1 Prior uncertainty

The uncertainty in the prior emissions determines how much the posterior is able to deviate from the prior. In LUMIA, the prior uncertainty is described by the prior error covariance matrix ($\boldsymbol{B}$) constructed with the correlation length approach. Each element of $\boldsymbol{B}$ (Eq. 2), i.e. the covariance between two elements of the control vector, is defined by Eq. 4. (Monteil and Scholze, 2021).

$$cov(\boldsymbol{x_1}, \boldsymbol{x_2}) = \sigma_{\boldsymbol{x_1}} * \sigma_{\boldsymbol{x_2}} * e^{-distance(p_1,p_2)/L_x} * e^{-|t_1-t_2|/L_t} \tag{4}$$

Here, a control vector elements $\boldsymbol{x_i}$ have spatial and temporal position p_i and t_i. The standard deviation $\sigma_{\boldsymbol{x_i}}$ is set to the the magnitude of the emissions at that point. The covariance exponentially decays with the distance between $\boldsymbol{x_i}$ and $\boldsymbol{x_j}$ both in space and time, scaled by correlation length L_x in space and L_t in time. With this formulation, the total uncertainty is sensitive to both correlation lengths and model resolution. Therefore, we scale the prior standard deviations, such that the computed total annual uncertainty equals the prescribed annual uncertainty (the choice of which is justified in Sect. 5.2.1).

https://doi.org/10.5194/egusphere-2025-1568
Preprint. Discussion started: 30 July 2025

3.2 Observational network

The observations of atmospheric BC used in the inversion were retrieved at Level-2 quality controlled level from the EBAS database of atmospheric composition monitoring (http://ebas.nilu.no, last access: 15 January 2025). In total, the inversion uses observations from 24 sites. Table 2 presents an overview of the sites and Fig. 1a presents their spatial distribution, while Fig. 1b shows the average sensitivity of the network. Only rural or semi-rural (two sites) sites were selected.

All observations assimilated in this study work on the principle of measuring the light absorption coefficient of a collected sample of aerosols. The coefficient is converted to concentration using the wavelength dependent mass absorption coefficient (MAC). The resulting concentration is referred to as equivalent BC (eBC) (Petzold et al., 2013). Here, we assume a MAC of 10 $\pm$ 1.33 m^2g^{-1} at 637 nm reported to be representative for a well mixed boundary layer in European background sites (Zanatta et al., 2016). We also assume no change in MAC from different sources, i.e. an Ångström exponent (AAE) equal to one (Zotter et al., 2017). With this assumption, MAC values at different wavelengths are extrapolated according to $MAC_\lambda = 10(637/\lambda)$ (Lack and Langridge, 2013).

Nine sites utilized the Multi Angle Absorption Photometers Model 5012 (MAAP-5012) by Thermo Scientific (Petzold and Schönlinner, 2004). This instrument measures the light absorption coefficient of aerosol samples using a light source with a wavelength of 670 nm. However, subsequent studies revealed the actual wavelength to be 637 nm (Zanatta et al., 2016). Still, most sites reported absorption coefficients at 670 nm. One site employed Particle Soot Absorption Photometers (PSAP-3W) by Radiance Research (Bond et al., 1999; Sinha et al., 2017). This instrument operates at three wavelengths between 470 and 660 nm. In addition, five sites used Continuous Light Absorption Photometers (CLAP-10) by NOAA (Ogren et al., 2017). The CLAP-10 operates at three different wavelengths between 467 and 652 nm. The present study utilizes the longest available wavelength for these instruments.

Finally, the Aethalometer by Magee Scientific was operational at eight sites (AE33) and one site (AE31) (Hansen et al., 1984; Drinovec et al., 2015). Both AE31 and AE33 measure the absorption of aerosol samples at seven different wavelengths ranging from 370 to 950 nm. Here, we define the concentration eBC by the absorption at 880 nm. The AE33 has been shown to consistently overestimate eBC concentrations compared to MAAP due to filter loading effects. Consequently, ACTRIS recommends applying a Harmonization factor of either 1.76 or 2.21 depending on filter type (Müller and Fiebig, 2021). The application of this factor, along with accompanying metadata, was inconsistent for 2021. Therefore, we cross-referenced with data providers and compared with forward model simulations and concluded that the factor (1.76) needed to be applied manually for five sites (*hpb*, *kos*, *rig*, *pay* and *pmi*, see Table 2).

The level-2, quality controlled, measurements retrieved from the EBAS database have a one-hour resolution (arithmetic mean of original sampling). The instrument uncertainty, the typical unit-to-unit variability (δ_{inst}), was in most cases reported in the metadata as a fraction, ranging from 5% to 25%. The observational uncertainty, σ_y, is derived from the instrument uncertainty as well as the MAC uncertainty, according to Eq. 5. For all measurements below the limit-of-detection (LOD), we assume a measurement value and uncertainty of LOD/2. This approach mimics the assumption that a measurement below the LOD can be any value from zero to the LOD, in the absence of the option to assume uniformly distributed measurements.

https://doi.org/10.5194/egusphere-2025-1568
Preprint. Discussion started: 30 July 2025

$$\sigma_y = y\sqrt{\frac{\sigma_{MAC_\lambda}}{MAC_\lambda}^2 + \delta_{inst}^2} \tag{5}$$

In line with Monteil and Scholze (2021), we selected a subset of the original observations for which the transport model is expected to perform optimally. One of the primary difficulties of transport modeling is accurately representing vertical mixing in the lower troposphere. This representation error is expected to be minimal either in a well-developed boundary layer (typically occurring in the afternoon) or well above the boundary layer (typically occurring at night for high-altitude sites). Therefore, the final observational dataset includes only observations between 12:00—18:00 local time for sites at lower altitudes (< 1000 m) or between 00:00—04:00 local time for high altitude sites (> 1000 m). The number of observations used for each site is presented in the last column in Table 2.

4 Inversion setup

The observations assimilated in this study are from the year 2021. Consequently, the emissions are optimized at daily resolution between 1 of January and 15th of December 2021. This ensures that there are observations available to constrain the entire solution. The domain is the same as the transport model: 15° W—35° E, 33—73° N with a resolution of 0.25°.

We first perform a set of synthetic inversions to evaluate the inversion framework's ability to recover a known set of emissions. Synthetic observations are generated by forward transport from the "truth", in our case the modified HTAPv3 emissions, combined with random noise to mimic observational error. The random noise is sampled from $\mathcal{N}(0, \sigma_y^2)$, where σ_y^2 is the observational error of the equivalent real observation (Eq. 5). In the synthetic experiment the CAMS-GLOB-ANTv5.3 emissions are used as the prior. The top section of Table3 lists the synthetic experiments and their different setups, starting with the synthetic base case (*SBase*) followed by the sensitivity test performed and how they differ from the base case.

The sensitivity towards the observation error is tested by applying a factor of 0.5 and 2 to the observation error (denoted as *SO.*). Then, we test the sensitivity towards the somewhat arbitrary choices of correlation lengths. First, by changing the horizontal correlation length L_x from 500 to 250 and 1000 km (*SCx.*), and then by changing L_t from 14 to 7 and 21 days (*SCt.*). The sensitivity towards the prescribed annual uncertainty in the prior emissions, 30 Gg in the base case, is evaluated by assuming annual uncertainties of 15 Gg and 60 Gg of BC (*SP.*).

Next, a set of inversions using the real observations is performed. The equivalent sensitivity experiments to the synthetic experiment are performed for the real inversions. The real sensitivity experiments are named analogues to the synthetic but with the first letter *R* instead of *S*, and are presented only in Appendix B1. Finally, two different ensembles of real inversions (described in Sect. 4.1) are computed to quantify the uncertainty in the real inversion.

For all experiments, we use the Root Mean Square Error normalized with the spread in the measurements (nRMSE) and the Pearson's correlation coefficient (r) as evaluation metrics when comparing the modeled eBC concentrations with the measurements. These metrics are computed for each site individually, and when averaged across all sites, they are weighted by the

https://doi.org/10.5194/egusphere-2025-1568
Preprint. Discussion started: 30 July 2025

Table 2. Observational sites and their metadata used in the inversion

Site ID	Name	Longitude	Latitude	Altitude	Instrument	Wavelength	Nr obs
arn	El Arenosillo	6.73°W	37.10°N	41 m	CLAP-10	652 nm	1995
beo	BEO Moussala	23.58°E	42.17°N	2925 m	CLAP-10	652 nm	1296
bir	Birkenes II	8.25°E	58.39°N	220 m	PSAP-3W	660 nm	1986
dem	DEM Athens	23.82°E	37.99°N	270 m	AE33	880 nm	2074
glh	Giordan Lighthouse	14.22°E	36.07°N	167 m	MAAP-5012	670 nm	1048
hac	Helmos Mountain	22.20°E	37.98°N	2314 m	CLAP-10	652 nm	886
hpb	Hohenpeissenberg	11.01°E	47.80°N	975 m	MAAP-5012	670 nm	2096
htm	Hyltemossa	13.42°E	56.10°N	115 m	AE33	880 nm	1308
hyy	Hyytiälä	24.28°E	61.85°N	181 m	CLAP-10	652 nm	2049
ipr	Ispra	8.64°E	45.81°N	209 m	MAAP-5012	670 nm	2181
jfj	Jungfraujoch	7.99°E	46.55°N	3578 m	AE33	880 nm	1117
kos	Kosetice (NAOK)	15.08°E	49.57°N	535 m	AE33	660 nm	2007
kps	K-puszta	19.58°E	46.97°N	125 m	CLAP-10	652 nm	642
mel	Melpitz	12.93°E	51.53°N	87 m	MAAP-5012	670 nm	1793
msa	Montsec	0.73°E	42.05°N	1571 m	MAAP-5012	670 nm	1258
neu	Neuglobsow	13.03°E	53.17°N	62 m	MAAP-5012	670 nm	1978
ope	Obs. Perenne de l'Environnement	5.51°E	48.56°N	396 m	AE31	880 nm	1667
pal	Pallas (Sammaltunturi)	24.12°E	67.97°N	560 m	MAAP-5012	637 nm	2083
pay	Payerne	6.94°E	46.81°N	489 m	AE33	880 nm	2181
pmi	Pic du Midi	0.14°E	42.94°N	2889 m	AE33	880 nm	1043
puy	Puy de Dôme	2.96°E	45.77°N	1465 m	MAAP-5012	670 nm	1133
rig	Rigi	8.46°E	47.07°N	1031 m	AE33	880 nm	1437
vda	Villeneuve d'Ascq	3.14°E	50.61°N	90 m	AE33	880 nm	2146
wal	Waldhof	10.76°E	52.80°N	74 m	MAAP-5012	670 nm	2047

number of observations. Eq. 6 defines nRMSE, where y and o represent the model and measurements of eBC.

$$nRMSE = \frac{\sqrt{\sum_{i=i}^{n} \frac{1}{n}(y_i - o_i)^2}}{o_{max} - o_{min}} \quad (6)$$

https://doi.org/10.5194/egusphere-2025-1568
Preprint. Discussion started: 30 July 2025

Table 3. List of experiments performed in this study

Experiment name	Prior	Prior annual uncert	Obs	Obs error fac	L_x	L_t
SBase	CAMS-GLOB-ANT	30 Gg	synthetic	1	500 km (exp)	14 days
SO.x05	-	-	-	0.5	-	-
SO.x2	-	-	-	2	-	-
SP.15	-	15 Gg	-	-	-	-
SP.60	-	60 Gg	-	-	-	-
SCx.250	-	-	-	-	250 km (exp)	-
SCx.1000	-	-	-	-	1000 km (exp)	-
SCt.7	-	-	-	-	-	7 days
SCt.21	-	-	-	-	-	21 days
RBase	HTAPv3, mod	30 Gg	real	1	500 km (exp)	14 days
REns	HTAPv3, mod, perturbed	-	real, perturbed	-	-	-
RCV	-	-	real, cross-validation	-	-	-

4.1 Uncertainty quantification

Firstly, we create an ensemble of sensitivity tests (real ensemble, *REns*) by perturbing the prior emissions and the observations. The standard deviation between the members, σ_{REns}, thus represent the uncertainty in the posterior emissions due to both bottom-up and observational uncertainty. Each member is initialized with observations deviating randomly from the reference by one standard deviation (the prescribed observational error, σ_y) and each element in the preconditioned control vector (ω, see Sect. 2) is set to a normal distributed random value between -1 and 1. Since the preconditioned control vector encodes the error covariance matrix, the resulting perturbations on the prior are spatially and temporally consistent. In total, the ensemble consists of 50 members. This was sufficient to recover the prescribed annual uncertainty in the prior (described in Sect. 3.1.1) in all cases.

Secondly, a cross-validation experiment is performed (real cross-validation, *RCV*). One site at a time is removed and kept for independent validation, resulting in 24 different inversions. The main purpose of the cross-validation is to validate the system with independent observations, but it also functions as a sensitivity test towards single sites and allows us to quantify the uncertainty due to changes in the observational network, σ_{RCV}. Since σ_{REns} and σ_{RCV} should be mostly independent and represent different types of uncertainties, we estimate the total uncertainty of the base inversion according to Eq. 7. Note that the inversion uncertainty due to the transport model is not assessed in this study.

$$\sigma_{RBase} = \sqrt{\sigma_{RCV}^2 + \sigma_{REns}^2} \tag{7}$$

https://doi.org/10.5194/egusphere-2025-1568
Preprint. Discussion started: 30 July 2025

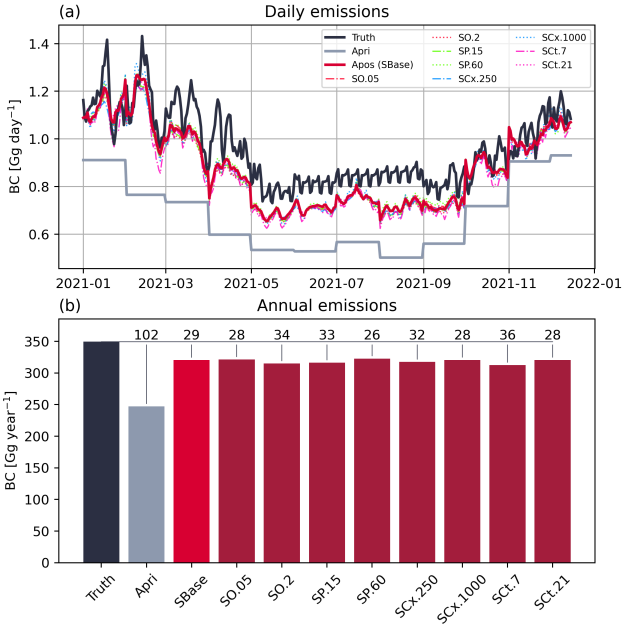

Figure 2. Daily emissions of 2021 (**a**) for prior (gray), truth (black) and posterior base case (red, solid) and posterior sensitivity tests (red, dashed) aggregated over the domain. Same data annually aggregated (**b**) with difference compared to truth annotated.

5 Results

5.1 Synthetic inversions

Figure 2 illustrates the daily and annual true, prior and posterior emissions aggregated over the domain. The base inversion (*SBase*) successfully recovers most of the annual emissions, with the annual bias decreasing from -102 Gg of BC (29% of the truth) in the prior compared to -29 Gg (8%) in the posterior. Additionally, part of the temporal variability of the true emissions is recovered, particularly the larger fluctuations. For instance, the rapid changes in February, late March, and October are captured. However, smaller-scale variability is not as well recovered, which can be attributed to the temporal correlation always being longer than a week. This includes the intra-weekly variability dominating the true emissions from May to September, which is also the period with the largest bias between the true and posterior emissions. Some major peaks, such as those in mid-January and early April, are also not recovered. Furthermore, the inversion results in an improved fit to the observations (Appendix A).

5.1.1 Sensitivity to inversion settings

The annual emissions of the sensitivity tests vary at most between -2 to 3% compared to the base posterior (Fig. 2b). The sensitivity tests demonstrate that the inversion is robust to observational and prior uncertainty; with half the observation uncertainty the posterior increases by 1 Gg (*SO.05*) and with twice the uncertainty it decreases by -5 Gg (*SO.05*). Halving the prescribed prior annual uncertainty reduces the posterior emissions by -4 Gg (*SP.15*), while doubling it results in an increase of

https://doi.org/10.5194/egusphere-2025-1568
Preprint. Discussion started: 30 July 2025

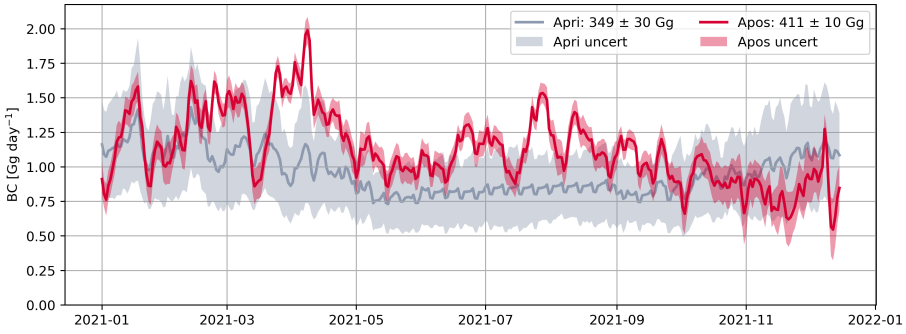

Figure 3. Daily emissions of 2021 for prior (gray), posterior RBase (red). The shaded area are the respective uncertainty represented as the standard deviation from ensemble of prior (σ_{REns}) and posterior (σ_{RBase}, Eq. 7). Annotated are the annually aggregated emissions with one std

3 Gg (*SP.60*). In practice, decreasing observational error or increasing prescribed prior annual uncertainty has the same effect; the cost function (Eq. 2) is dominated by the right term, allowing for a better fit to the observations, and thus resulting in a larger deviation from the prior. Changing the correlation lengths results in changes of similar magnitude, further indicating the robustness of the inversion. The largest deviation, -7 Gg, occurs when decreasing temporal correlation from 14 to 7 days (*SCt.7*). The daily emissions of the sensitivity tests (Fig. 2a), dashed and dotted lines) reflect the robustness of the inversion, as the sensitivity tests follow the base inversion with a maximum of -7% deviation occurring in February (*SCt.7*).

5.2 Real inversions

Figure 3 presents the daily and annual emissions (annotated) of the prior and posterior aggregated over the domain. Annually, the real base inversion (*RBase*) results in 411 $\pm$ 10 Gg of emitted BC from anthropogenic sources (with standard deviation from Eq. 7). This represents an 18% increase over the prior annual emissions of 349 $\pm$ 30 Gg. The increase in emissions occurs predominantly in late March until October, while the emissions are on average similar for the late autumn and winter months.

The spatial distribution of the annual emissions is presented in Fig. 4 for the prior (a), posterior (b), and difference (c). Most of the spatial features of the prior are preserved in the posterior, with high emissions in Central England, Southwest Netherlands, Po Valley, Southern Poland, Central Balkans, as well as major cities. The posterior emissions are generally higher across the domain, with reductions limited to Northwestern Europe and Northern Poland. The largest increases are observed in the Po Valley, Central Europe, Iberian Peninsula, and Balkans.

In addition, Fig. 4 presents the relative uncertainty in the prior (d), and posterior emissions (e). The nearly uniform relative uncertainty of the prior is reduced in the inversion, especially in the vicinity of measurement sites, with some exceptions. In areas where the posterior emissions are lower, the relative uncertainty is higher, such as around Italy and the Netherlands. Theoretically, for any one inversion, the absolute uncertainty should not increase, however since we evaluate the uncertainty based on an ensemble it can happen if the different inversions converge on different solutions. Figure 4f) illustrates the absolute difference between posterior and prior uncertainty relative to the prior emissions. The reduced uncertainty correlates spatially

https://doi.org/10.5194/egusphere-2025-1568
Preprint. Discussion started: 30 July 2025

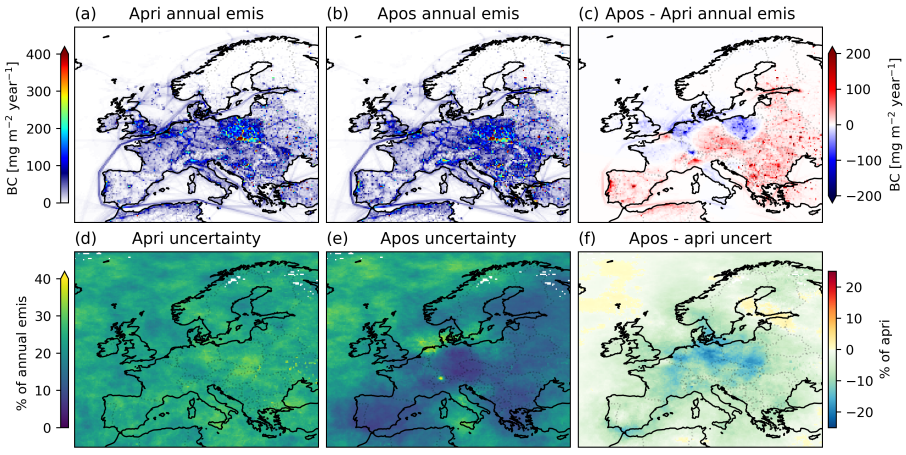

Figure 4. In upper row, the prior (**a**), base posterior (**b**) 2021 emissions and the difference (posterior-prior, **c**). Their respective uncertainty, i.e. the standard deviation of the ensemble (*REns*), as a percentage of the prior (**d**) and posterior (**e**) emissions as well as the difference in uncertainty with respect to the prior emissions (**f**).

with the density of the measurement sites and, consequently, the network sensitivity (see Fig. 1), showing a reduction in Central Europe but essentially no change around the periphery, especially in Southern Finland. Both of σ_{REns} and σ_{RCV} are lower in the center of the domain (not shown). Therefore, the overall spatial posterior standard deviation results in a near net-zero change on the periphery. This clearly illustrates the added value of having more observation sites in the periphery of the (European) domain.

The seasonal variations of the prior and posterior emissions as well as the emission and uncertainty difference are presented in Fig. 5. In winter (DJF), the prior has very high emissions in Southern Poland compared to the rest of the domain. The base inversion reduces emissions in Poland, France, and Italy while increasing emissions around Germany, the Czech Republic, the Po Valley, and Eastern Europe. The result is a more uniform posterior in Central Europe. This is not the case for spring (MAM), where the prior emissions are much lower in Poland. The posterior emissions in Poland are more similar to winter, resulting in a widespread increase in most of Central and Eastern Europe, with lower emissions only in Italy, Northwestern Europe, and the Baltic coast of Poland. A similar pattern occurs in summer (JAJ), but with a southerly shift of the increased emissions to the Mediterranean region. A small but substantial emission decrease occurs in Switzerland. The autumn (SON) prior and posterior emissions are very similar to the winter months, but with larger reductions in Poland and the Baltics. The lower posterior emissions in Northwestern Europe remain throughout the year. The uncertainty relative to the prior is similar to the annual aggregated data, but with overall larger reductions both in terms of magnitude and spatial extent.

5.2.1 Sensitivity and uncertainty

From the real ensemble experiment (*REns*), we quantify the sensitivity of the inversion and the associated uncertainty to prior emissions and observations. With the prescribed prior annual uncertainty of 30 Gg, the resulting ensemble spread of priors is

https://doi.org/10.5194/egusphere-2025-1568
Preprint. Discussion started: 30 July 2025

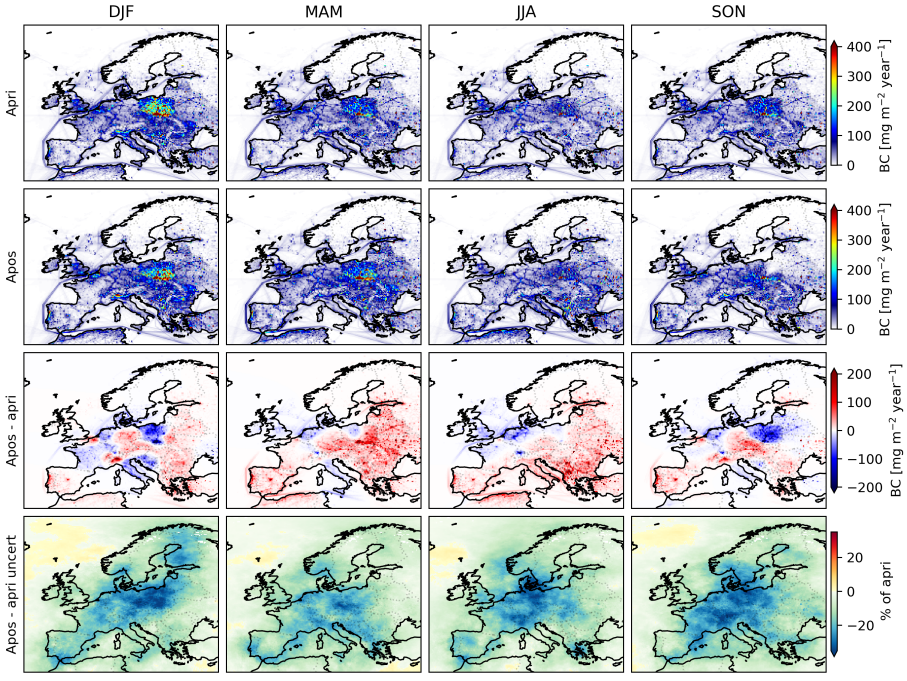

Figure 5. The seasonal variation, columns, of the same variables as Fig. 4a-c,f) in the rows.

154 Gg (270—424 Gg, min to max). This range effectively covers the spread between different bottom-up emission estimates in the domain. For instance, the difference between the EMEP (Ullrich et al., 2023) and CAMS-GLOB-ANTv5.3 (Sect. 3.1) bottom-up inventories in the domain is 172 Gg for 2021. This confirms that the rather arbitrary choice of 30 Gg in annual prior uncertainty is realistic. The ensemble spread of posterior emissions is 27 Gg (ranging from 398—425 Gg) with a standard deviation (σ_{REns}) of 7 Gg. This represents a reduction in spread by approximately 80%, indicating that the inversion is very robust with respect to both prior emissions and observations.

The cross-validation experiments (*RCV*) provide a quantified sensitivity of the inversion to the observational network. Figure B2 shows the daily and annual posterior emissions for each inversion in the cross-validation. We observe that the largest changes occur when sites that are mostly influenced by emissions at the boundary are excluded. Removing single sites where the network density is high has a much smaller effect on the annual emissions. Overall, the sensitivity due to observational network results in a spread of 37 Gg (394—431 Gg) with a standard deviation (σ_{RCV}) of 8 Gg.

In general, the inversion is robust with respect to the prior emissions and observations as well as the observational network, especially where it is dense. Removing single sites in areas outside of dense regions can result in the largest deviations. We assume that the uncertainties from *RCV* and *REns* represent the uncertainty of the base inversion due to prior emissions, observations, and the site network, and that they are independent. Consequently, we estimate σ_{RBase} (Eq. 7) to be 10 Gg, 67% less than the prescribed uncertainty of the prior. The sensitivity of the real inversion due to inversion settings is similar to the synthetic experiment (Sect. 5.1.1), resulting in changes ranging from -3.6% to 2.4% from *RBase* (Fig. B1).

https://doi.org/10.5194/egusphere-2025-1568
Preprint. Discussion started: 30 July 2025

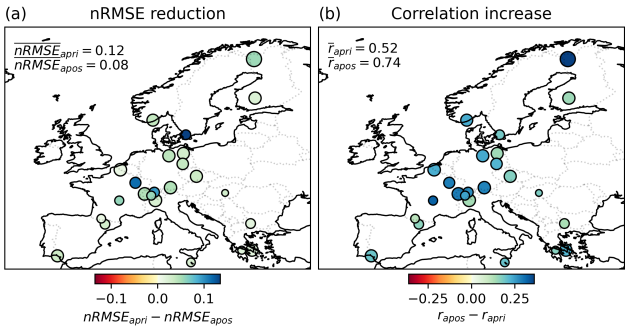

Figure 6. Diagnostics of the real base inversion (*RBase*) by comparing the site specific modelled BC concentrations from prior and posterior emissions to the dependent observations. The nRMSE reduction (**a**) and correlation increase (**b**) of the base posterior compared to the prior at each of the sites. The sizes of the dots is proportional to number of observations. The annotated values are the averages, weighted by number of observations.

5.2.2 Improved observational fit

Comparing the modelled observations from the prior and posterior emissions to the observations is a common method for diagnosing inversions (Michalak et al., 2017). In the real base inversion, the prior emissions underestimate the mean eBC by -23%. This bias is reduced to -14% in the real base posterior emissions. The site-specific reduction in normalized Root Mean Square Error (nRMSE) and increase in correlation is presented in Fig. 6. The correlation increase is relatively uniform. In contrast, there is a tendency for a larger reduction in nRMSE in the central domain. The largest reduction occurs at Hyltemossa (*htm*) and the least at Villeneuve d'Ascq (*vda*). The averaged metrics, weighted by the number of observations, are annotated in the respective Fig. and show that the base real inversion (*RBase*) is fitting the observations better. The network averaged nRMSE and correlation coefficient (annotated in Fig. 6) show an improvement of -33% and +40% respectively in the posterior concentrations.

5.2.3 Cross-validation

Ideally, to validate the posterior, independent observations which are not used in the optimization should be used. However, each observation left for evaluation is an observation not assimilated in the posterior. Therefore, we opted for a cross-validation scheme with multiple inversions, leaving one site for validation each time. There are 24 sites, resulting in 24 inversions. Note that this approach does not validate the exact posterior where all sites are assimilated, i.e. the real base inversion (*RBase*), but rather validates similar posteriors and assesses the sensitivity to single sites. It also indicates how the base inversion is expected to perform on new observational data, given their area of influence.

Figure 7 presents the fit to the independent observations for each site and networked averaged in the cross-validation as measured by nRMSE (a,d) and correlation coefficient (c,e). On averaged, the nRMSE is 1.7% lower in the posterior while the

https://doi.org/10.5194/egusphere-2025-1568
Preprint. Discussion started: 30 July 2025

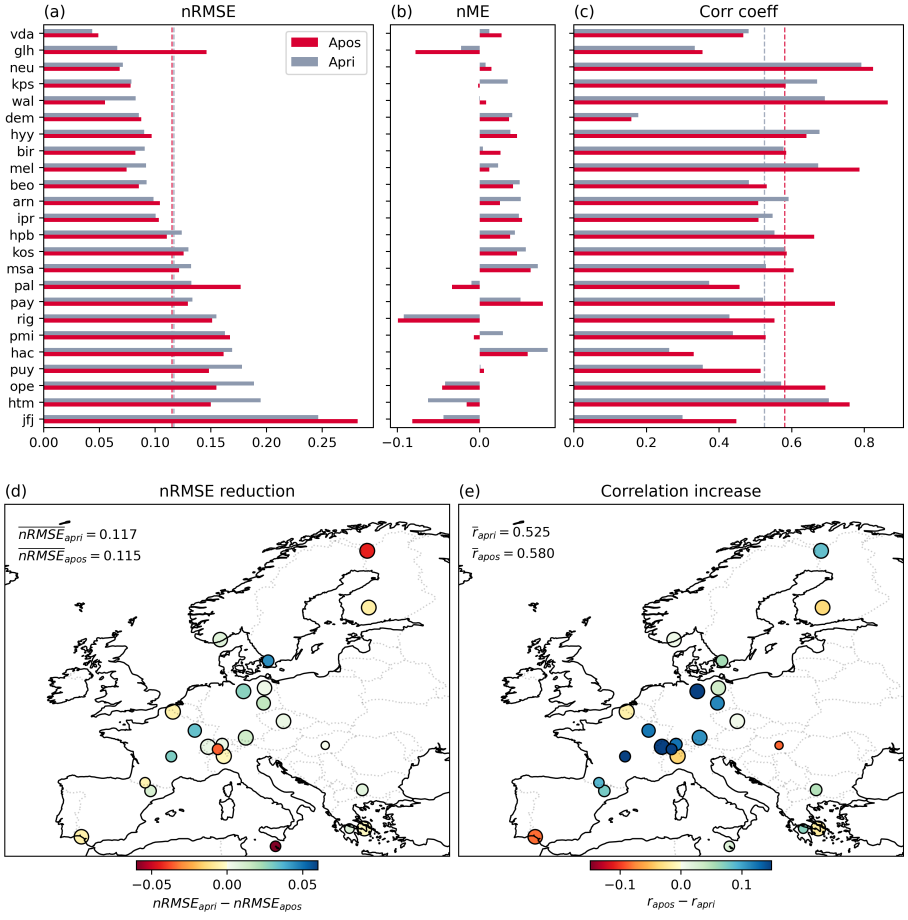

Figure 7. Observational fit from cross-validation experiment for each site. In upper row the absolute values of posterior and prior nRMSE (**a**), nME (**b**) and correlation coefficient (**c**). In bottom row, the nRMSE decrease (apri-apos, **c**) and correlation increase (apos-apri, **d**). Note that for the posterior metrics, the posterior is first generated with an inversion with all but the labelled site assimilated and then the observations at the site are evaluated with a forward run, i.e. the posterior metrics represent independent validation. The sizes of the dots is proportional to number of observations. The site averaged nRMSE and r, weighted by number of observations for are annotated and presented with dashed lines.

correlation increases by 10.5%. A majority of sites show a reduced nRMSE (15 out of 24) and increased correlation (18). Only three sites show a significantly worse nRMSE, namely Giordan Lighthouse (*glh*), Pallas (*pal*) and Jungfraujoch (*jfj*).

When sites far away from other sites or sites sensitive to emissions at the domain edge (e.g., isolated sites or alpine sites) are removed, the posterior tends to perform worse compared to the prior. This includes (but is not limited to) the three sites listed above. The poorer performance of isolated sites in these cross-validation experiments highlights the importance of a high-density observational network and suggests that care should be taken when analyzing the real base (*RBase*) emissions (or any other BC emissions optimized with surface observations) in areas far from the assimilated sites' sensitivity. It also

https://doi.org/10.5194/egusphere-2025-1568
Preprint. Discussion started: 30 July 2025

indicates that the inversions tend to use emissions at the "entry point" of particles over the continent to correct various biases (e.g., from the boundary condition). In the absence of observational constraints, the inversion can apply changes more freely here. Therefore, these peripheral sites are crucial for ensuring accurate resolution of emissions in the core part of the domain, but the emissions in the peripheral regions remain (more) uncertain.

Additionally, the normalized mean error (nME, $\frac{\bar{o}-\bar{y}}{o_{max}-o_{min}}$) is presented (Fig. 7b). The prior is, on average, overestimating the measurements at only six sites (negative nME). The remaining sites cause the inversion to increase emissions (positive nME). Therefore, it is not surprising that independently evaluating sites with the opposite signal, which are isolated, results in a worse posterior fit. All three of the worst-performing sites in the cross-validation (*glh*, *pal* and *jfj*) have a negative nME. Since no other site is sensitive enough to emissions in the same regions as these, the inversion does not have the necessary information to correct for the opposing bias when any of these sites are not assimilated. The remaining sites with negative nME are mostly sensitive to emissions in the same area, thus this is not an issue, and the posterior nRMSE is improved. At the same time, we see that the correlation is not affected by the opposing nME signals, since the correlation coefficient is independent of any absolute biases. The higher correlation of the posterior at most sites in the central domain suggests that the information about the temporal variability that the inversions use to improve the correlation is uniform between sites.

6 Discussion

The total annual posterior emissions of 411 $\pm$ 10 Gg are higher than both the prior and most other available bottom-up estimates for the domain and year, suggesting a general underestimation in the bottom-up inventories. This is particularly evident when comparing with the CAMS-GLOB-ANTv3, which estimates annual emissions of around 227 Gg. The posterior emissions are closest in magnitude to the EMEP (Ullrich et al., 2023) bottom-up emissions of 399 Gg. However, spatially and temporally there are still significant differences between the posterior and EMEP emissions.

Compared to the prior emissions, the the annual posterior emissions are around 18% higher. During winter time, a period when emissions of BC in Europe is dominated by residential combustion, the prior and posterior agree well. This suggests that this sector is well represented in the bottom-up emissions. However, this is probably not uniform in all countries as we note that in Poland specifically, a country with high emissions in this sector, the posterior suggests significantly less emissions. We found higher emissions in spring, mostly in Eastern Europe. A possible cause of this could be open burning of agricultural residue, which is banned in all EU countries but it is still being practiced in this area (Hall et al., 2021). The burned area (and consequently bottom-up estimated emissions) can be underestimated, partly due to the small scale of each fire and partly due to not being officially reported (Hall et al., 2021). The present study covers a complete year, but to further investigate the extent of the bottom-up underestimation and its underlying causes, future work will include a multi-year inversion with the inversion setup described and validated in this study.

To our knowledge, there are no other top-down BC emission estimates covering the same region for recent years, making inter-comparison impossible. However, we can compare our posterior emissions with top-down emission estimates for the period Jan—April 2020, on a slightly larger domain from Evangeliou et al. (2021). For that period, Evangeliou et al. reports

https://doi.org/10.5194/egusphere-2025-1568
Preprint. Discussion started: 30 July 2025

191 Gg. During the equivalent period in 2021, our top-down emissions results in 159 Gg of emitted BC. Considering the smaller domain of the present study, the estimates are in agreement despite using priors of very different magnitude. However, the estimate of Evangeliou et al. (2021) includes a reduction of around 46 Gg compared to the previous five years, about half of which is contributed by the COVID-19 pandemic. How those effects are carried into 2021 is not explored, but in early 2021 there was still restrictions in some countries.

Both Evangeliou et al. (2021) and this study are based on a very similar setup of FLEXPART to model the transport of BC in the atmosphere, which might be part of the reason why they seem to agree. Indeed, the posterior sensitivity to the transport model is the main factor of potential uncertainty not explored or quantified in the present study. In future studies, one option is to alter the FLEXPART settings, which have been shown to result in larger uncertainty than using different prior emissions (Evangeliou et al., 2018). Another option for future work would be to compare with a different transport model altogether. Using a different transport model is also preferred for future validation of the top-down estimates.

Our approach of assessing posterior uncertainties is to our knowledge a novel implementation in the field of aerosol (BC) inversions. We recommend future work to utilize this approach for three reasons: 1) by perturbing both observations and prior emissions in the same inversions we get information about the uncertainty due to these factors at the same time. 2) the cross-validation scheme provides information about the effect of the observational network on uncertainty while 3) acting as a method of general validation without the need to withhold assimilated observation.

6.1 Effects of wildfires and background emissions

As in any atmospheric inversion, completely separating different sources is not possible, since the system cannot distinguish between the sources if they are collocated in space and time. In the context of the present study, we cannot be certain that the posterior only includes anthropogenic sources. However, the vast majority of changes between the prior and posterior emissions described in this study are in the anthropogenic sectors. The prescribed wildfire emissions are only 1.4% of the prescribed anthropogenic emissions within the European domain (Table 1). Even if the prescribed wildfire emissions (see Table 1), which is based on satellite observations, are incorrect by a large fraction, the changes between the prior and posterior are still larger. In addition, the wildfire contribution to BC concentration is considered throughout the inversion (non-optimized sector).

We can compare the contribution of the wildfire emissions in the domain to the modelled observations. Network averaged, they contribute only 0.5% to the average posterior modelled concentrations of 0.20 μg m^{-3}. Most wildfires in the domain occur in the eastern and southern part, far away from most of the sites. The site with the largest contribution from wildfires (3.5%) is DEM Athens (*dem*) with 3.5% of the modelled BC concentration.

In contrast, there is a larger contribution from emissions, both anthropogenic and wildfires, outside the domain (y^{bg}, see Sect. 2.2). Network averaged, y^{bg} is 10.2% of the total modelled concentration, with sites at high altitude being more significantly influenced. At most, 52% of the average concentration is attributed to y^{bg} at Jungfraujoch (*jfj*) and Pic du Midi (*pmi*). Therefore, we recommend future BC inversions should consider the boundary conditions for this domain (or similarly sized domains), despite the short lifetime of BC in the atmosphere. Otherwise, the inversion will be biased to a solution of higher emissions.

https://doi.org/10.5194/egusphere-2025-1568
Preprint. Discussion started: 30 July 2025

6.2 Negative emissions

As mentioned in Sect. 3.1.1, negative emissions are mathematically plausible with the LUMIA inversion framework but physically unlikely. In total, the real base posterior emissions include -2.2 Gg (0.6% of the annual) of "negative" emissions. There are multiple ways of solving this issue. An inequality constraint can be applied to the posterior, essentially setting the negative emissions to zero but considering the posterior covariance matrix (Evangeliou et al., 2018, 2021; Jia et al., 2021). However, this approach infers a positive bias on any aggregated estimates. Another possible future improvement would be the implementation of a log-normally distributed control vector (Guerrette and Henze, 2017). However, considering their small magnitude, risk of otherwise introducing biases and technical limitations, the negative emissions are left as is in the present study.

7 Conclusions

This study presents the first application of the Lund University Inversion Algorithm to aerosol emissions. Specifically, anthropogenic black carbon emissions in Europe (15° W–35° E, 33–73° N) for 2021 are optimized by assimilating surface observations of equivalent black carbon from 24 ACTRIS and GAW background sites hosted on the EBAS database. The atmospheric transport model FLEXible PARTicle dispersion model (FLEXPART) is used to calculate the senstivity of observations to emission 14 days back in time in the inversion domain. The background concentrations are computed with transport 30 day backwards in the entire Northern Hemisphere. On average, the background concentrations, from both anthropogenic sectors and wildfires, are found to be 10.2% of the total. Therefore, we recommend future BC inversion studies of this, or similar sized domains, to consider background concentrations. In contrast, wildfire BC emissions within the domain contribute only 0.5%.

Synthetic inversions show that the framework is able to recover a prescribed true emission dataset well by reducing the annual bias by 72% and reconstructing large temporal variations. Intra-weekly variability is not as well recovered. Several sensitivity tests show that the inversion is robust with respect to inversion settings, both the synthetic and inversion with real observations.

The posterior annual emissions from the inversion with the real observations is found to be 411 ± 10 Gg of BC, which is 18% higher than the prior emissions as defined in our modified version of the HTAPv3 dataset with updated European emissions in line with official reporting. It is also higher than most other bottom-up inventories in the domain. Most of the increase occurs in April through September in the Eastern part of the domain and the Iberian peninsula. The largest emission reductions in the posterior are found in Poland during winter and autumn. While direct comparison to other top-down emission estimates is not possible, we find that our results are in agreements with findings from Evangeliou et al. (2021) in spring time.

We assess the uncertainty of the posterior with two ensembles of inversions, an implementation that we recommend future work to utilize. Firstly, an ensemble with perturbed prior and observations results in an annual emissions standard deviation of 7 Gg. This represents the uncertainty of the posterior due to the prior and observations. Secondly, a cross-validation scheme, where one site is removed at the time, provides an estimate of the uncertainty due the choice of sites. Annually, the resulting standard deviation is 8 Gg, with most of the variability occurring when isolated sites are removed. Spatially, the combined

https://doi.org/10.5194/egusphere-2025-1568
Preprint. Discussion started: 30 July 2025

uncertainty from both cross-validation and ensemble results in an overall reduction of uncertainty in the central part of the domain, where the observational network density is high.

Additionally, the cross-validation scheme is used to validate the posteriors with independent observations. In a majority of cases the posterior emissions result in modelled concentrations that fit the independent observations better. A worse observational fit was only observed when the not-assimilated site is both isolated and has an average signal opposite from other sites. Therefore, we argue that these sites are important to ensure an accurate resolution of the emissions in the core part of the domain, while the emissions in the peripheral regions remain uncertain and more observations would be needed in these areas to confidently reduce uncertainty there.

This work show that Black Carbon emissions in Europe are underestimated in bottom-up inventories for 2021. This have environmental impacts from a modelling perspective: less emissions in climate or atmospheric transport models may lead to underestimating of for example radiative forcing or air quality effects. In addition, this work is a first step in identifying what (missing or misrepresented) sectors in bottom-up inventories is the driver for this underestimation, information which can help guide future policy changes. At the same time, the results show that for certain regions and periods the top-down inventory instead can act as a verification that bottom-up inventories are indeed correct.

Finally, we discuss possibilities to improve the inversion setup further for top-down emissions estimates of BC, or other aerosol species with LUMIA. For instance, sensitivity towards the transport model is not assessed in this study. In addition, false "negative" emissions could be removed by applying an inequality constraint to the posterior or by assuming log-normally distributed emissions.

Code and data availability. The LUMIA source code is publicly available and can be downloaded from https://github.com/lumia-dev/lumia. FLEXPART is publicly available and can be downloaded from https://www.flexpart.eu/ (Pisso et al., 2019). Model output from all experiments and FLEXPART footprints are to large to upload, but can be accessed upon request to the corresponding author of this paper. Prior emission datasets are also available for download. Modified HTAPv3 at https://meta.icos-cp.eu/collections/npTsl_Y_k65gZtLSdVDHEs1o (Denier van der Gon et al., 2023), CAMS-GLOB-ANT at https://doi.org/10.24380/eets-qd81 (Soulie et al., 2024) and GFEDv4s at https://www.globalfiredata.org/ (van der Werf et al., 2017). The level-2 absorption coefficient measurements are available for download at https://ebas-data.nilu.no/. All results can also be accessed upon request to the corresponding author of this paper.

https://doi.org/10.5194/egusphere-2025-1568
Preprint. Discussion started: 30 July 2025

Appendix A: Diagnostic of synthetic experiments

Here we show the observational fit of the base synthetic inversion. Overall, the prior modelled BC concentrations underestimate the synthetic observations with -10%, which is decreased to -0.6% in the posterior emissions. The improvement in the fit to the observations is not uniform in the network, as illustrated by the reduction in nRMSE and the increase in correlation for each site in Fig. A1. Overall, there is a tendency for a better observational fit, i.e. larger reduction in nRMSE and increase in correlation, in the central domain. The averaged metrics, weighted by the number of observations, are annotated in the respective Fig. and show that the base synthetic inversion (*SBase*) is fitting the observations better. Compared to the prior, nRMSE of the posterior is reduced by 48% while correlation increased by 13% on average.

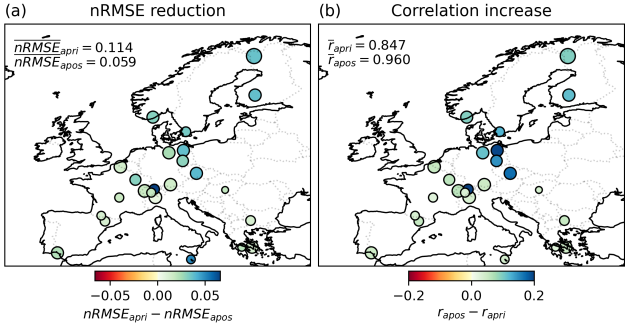

Figure A1. Diagnostics of the synthetic base inversion by comparing the site specific modelled BC concentrations from prior and posterior emissions to the dependent observations. The nRMSE reduction (**a**) and correlation increase (**b**) of the base posterior compared to the prior at each of the sites. The sizes of the dots is proportional to number of observations. The annotated values are the averages, weighted by number of observations.

https://doi.org/10.5194/egusphere-2025-1568
Preprint. Discussion started: 30 July 2025

Appendix B: Real inversion experiments

B1 Sensitivity to inversion setttings

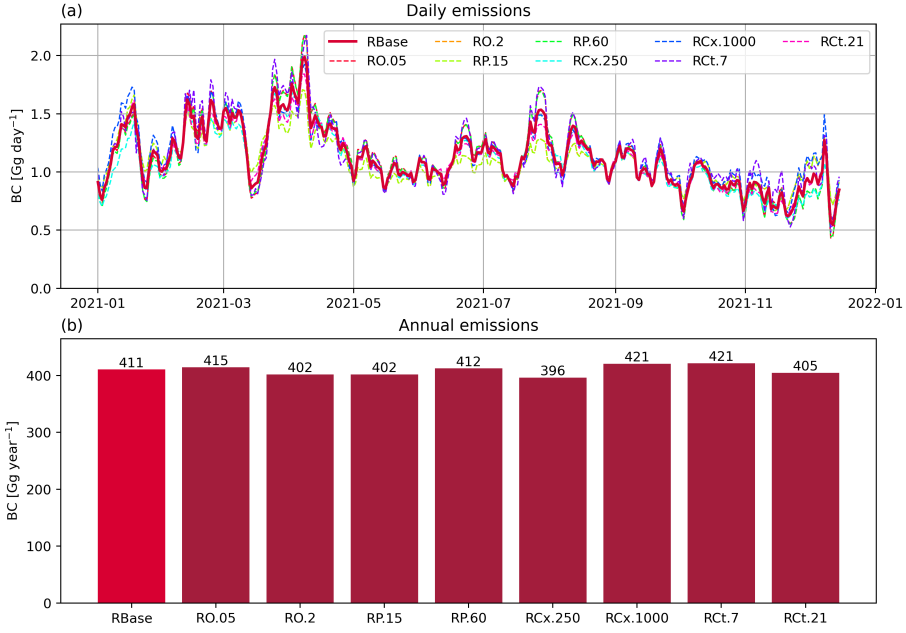

Figure B1. Upper row (**a**) shows daily emissions of 2021 for real base posterior *RBase* (red, solid) and posteriors from real sensitivity tests (dashed) aggregated over the domain. In the bottom row (**b**), the annually aggregated emissions. The sensitivity test are equivalent to the sensitivity tests of the synthetic experiments (Sect. 5.1.1).

The real base inversion (*RBase*) behaves very similar to the synthetic inversion (Sect. 5.1.1) when changing the inversion parameters, presented in Fig. B1. Overall, the annual posterior emissions vary between -3.6% to 2.4% from *RBase* in the sensitivity tests (Fig. 3b) indicating that the real inversion is rather robust to inversion settings. Changing both observational (*RO.05, RO.2*) and prescribed prior (*RP.15, RP.60*) uncertainty changes the emissions as expected, but less than the effects of changing the correlation lengths. Specifically, the inversion with the lowest spatial correlation (*RCx.250*) results in the lowest posterior, 15 Gg less than base. In contrast, with higher spatial or lower temporal correlation (*RCt.1000* and *RCt.7*) the posterior is the highest with 10 Gg more than the base inversion. The total in spread annual posteriors emissions due to inversion settings is 25 Gg (396–421 Gg, min to max).

https://doi.org/10.5194/egusphere-2025-1568
Preprint. Discussion started: 30 July 2025

B2 Cross-validation

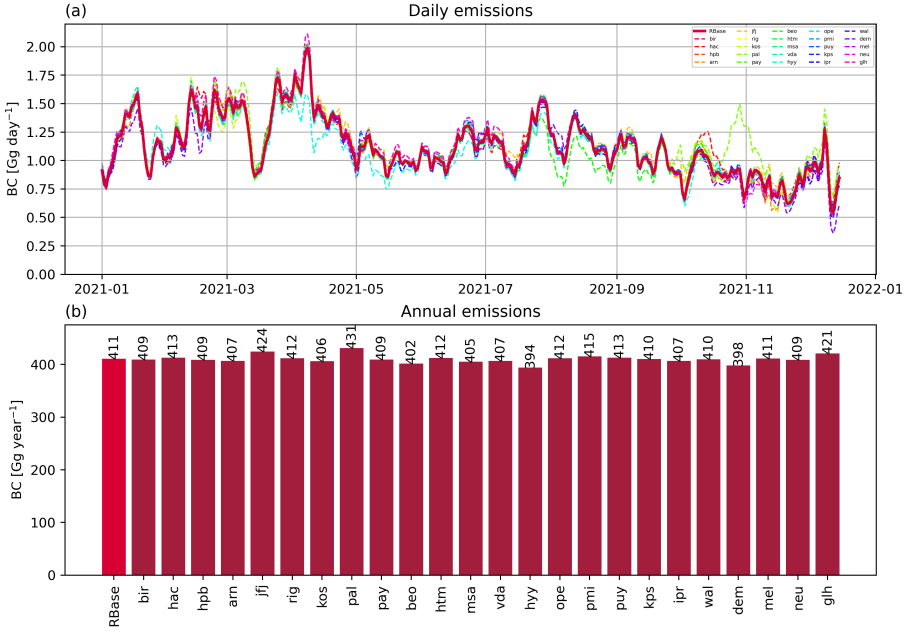

Figure B2. Upper row (**a**) shows daily emissions of 2021 for real base posterior *RBase* (red, solid) and posteriors from cross-validation (dashed) aggregated over the domain. In the bottom row (**b**), the annually aggregated emissions. For each CV posterior, the label shows which site is not included in the assimilation

While the main purpose of the cross-validation experiments (*RCV*) is to validate the inversion with independent observations (see Sect. 5.2.3), it also provides a quantified sensitivity of the inversion to the observational network. As mentioned, Fig. B2 presents the annual (a) and posterior (b) emissions for each inversion in the cross-validation, where the label shows which site is removed from the inversion. We note that the largest changes occur when sites close to the boundary (or sites that are influenced by emission at the boundary) are removed. For instance, the largest annual posterior emissions happen when sites like Pallas (*pal*, 431 Gg) or Jungfraujoch (*jfj*, 424 Gg) are not included in the inversions, while the smallest occurs when Hyytiälä (*hyy*, 394 Gg) is removed. Removing single sites where the network density is high have a much smaller effect on the annual emissions. Overall, the sensitivity due to observational network results in a spread of 37 Gg (394–431 Gg, min to max) with a standard deviation, σ_{RCV} of 8 Gg.

https://doi.org/10.5194/egusphere-2025-1568
Preprint. Discussion started: 30 July 2025

Author contributions. AT led the work in terms of conceptualization, formal analysis and investigation, with supervision from PR. MS, NS and BG were involved in developing the work throughout. GM developed the inversion model and provided technical support with transport modelling. HDG provided the prior emissions. AT prepared the original manuscript with review and editing contributions from all co-authors.

Competing interests. The authors declare no competing interests

Acknowledgements. The research is a part of the Swedish strategic research area: ModElling the Regional and Global Earth system (MERGE) and LTH Profile Area: AEROSOLS. We thank all the observation data providers and infrastructures (ACTRIS, GAW and EMEP) and we thank EBAS for collecting and distributing the observations. Extra thanks to Erik Alhlberg for supporting the process of correcting incomplete AE33 data and providing data for Hyltemossa. For aiding in cross-referencing of AE33 data we thank Joel F. de Brito (Villeneuve d'Ascq), Christoph Hueglin (Rigi and Payerene) and Saliou Mbenguw (Kosetice). We thank Jeroen Kuenen and Stijn Dellaert (TNO) for support with the modification of the HTAPv3 dataset.

All maps in this paper were made with Natural Earth.

Funding statement: This research is a part of the AVENGERS project, funded by European Union's Horizon Europe research and innovation programme under Grant Agreement No. 101081322. The computations and data handling was enabled by resources provided by LUNARC, The Centre for Scientific and Technical Computing at Lund University. Also by the National Academic Infrastructure for Supercomputing in Sweden (NAISS), partially funded by the Swedish Research Council through grant agreement no. 2022-06725.

https://doi.org/10.5194/egusphere-2025-1568
Preprint. Discussion started: 30 July 2025

References

Bond, T. C., Anderson, T. L., and Campbell, D.: Calibration and Intercomparison of Filter-Based Measurements of Visible Light Absorption by Aerosols, Aerosol Science and Technology, 30, 582–600, https://doi.org/10.1080/027868299304435, 1999.

Chen, C., Dubovik, O., Schuster, G. L., Chin, M., Henze, D. K., Lapyonok, T., Li, Z., Derimian, Y., and Zhang, Y.: Multi-angular polarimetric remote sensing to pinpoint global aerosol absorption and direct radiative forcing, Nature Communications, 13, 7459, https://doi.org/10.1038/s41467-022-35147-y, publisher: Nature Publishing Group, 2022.

Clarke, A. D. and Noone, K. J.: Soot in the Arctic Snowpack: A Cause for Perturbations in Radiative Transfer, Atmospheric Environment (1967), 19, 2045–2053, https://doi.org/10.1016/0004-6981(85)90113-1, 1985.

Cohen, J. B. and Wang, C.: Estimating Global Black Carbon Emissions Using a Top-down Kalman Filter Approach, Journal of Geophysical Research: Atmospheres, 119, 307–323, https://doi.org/10.1002/2013JD019912, 2014.

Crippa, M., Guizzardi, D., Butler, T., Keating, T., Wu, R., Kaminski, J., Kuenen, J., Kurokawa, J., Chatani, S., Morikawa, T., Pouliot, G., Racine, J., Moran, M. D., Klimont, Z., Manseau, P. M., Mashayekhi, R., Henderson, B. H., Smith, S. J., Suchyta, H., Muntean, M., Solazzo, E., Banja, M., Schaaf, E., Pagani, F., Woo, J.-H., Kim, J., Monforti-Ferrario, F., Pisoni, E., Zhang, J., Niemi, D., Sassi, M., Ansari, T., and Foley, K.: HTAP_v3 Emission Mosaic: A Global Effort to Tackle Air Quality Issues by Quantifying Global Anthropogenic Air Pollutant Sources, https://doi.org/10.5194/essd-2022-442, 2023.

Denier van der Gon, H., Kuenen, J., Dellaert, S., and Visschedijk, A.: Input Data for Aerosol Inversions, AVENGERS Deliverable 3.1, TNO, https://avengers-project.eu/outputs/, 2023.

Denier van der Gon, H. a. C., Bergström, R., Fountoukis, C., Johansson, C., Pandis, S. N., Simpson, D., and Visschedijk, A. J. H.: Particulate Emissions from Residential Wood Combustion in Europe – Revised Estimates and an Evaluation, Atmospheric Chemistry and Physics, 15, 6503–6519, https://doi.org/10.5194/acp-15-6503-2015, 2015.

Drinovec, L., Močnik, G., Zotter, P., Prévôt, A. S. H., Ruckstuhl, C., Coz, E., Rupakheti, M., Sciare, J., Müller, T., Wiedensohler, A., and Hansen, A. D. A.: The "Dual-Spot" Aethalometer: An Improved Measurement of Aerosol Black Carbon with Real-Time Loading Compensation, Atmospheric Measurement Techniques, 8, 1965–1979, https://doi.org/10.5194/amt-8-1965-2015, 2015.

Evangeliou, N., Thompson, R. L., Eckhardt, S., and Stohl, A.: Top-down Estimates of Black Carbon Emissions at High Latitudes Using an Atmospheric Transport Model and a Bayesian Inversion Framework, Atmospheric Chemistry and Physics, 18, 15 307–15 327, https://doi.org/10.5194/acp-18-15307-2018, 2018.

Evangeliou, N., Platt, S. M., Eckhardt, S., Lund Myhre, C., Laj, P., Alados-Arboledas, L., Backman, J., Brem, B. T., Fiebig, M., Flentje, H., Marinoni, A., Pandolfi, M., Yus-Dìez, J., Prats, N., Putaud, J. P., Sellegri, K., Sorribas, M., Eleftheriadis, K., Vratolis, S., Wiedensohler, A., and Stohl, A.: Changes in Black Carbon Emissions over Europe Due to COVID-19 Lockdowns, Atmospheric Chemistry and Physics, 21, 2675–2692, https://doi.org/10.5194/acp-21-2675-2021, 2021.

Guerrette, J. J. and Henze, D. K.: Four-Dimensional Variational Inversion of Black Carbon Emissions during ARCTAS-CARB with WRFDA-Chem, Atmospheric Chemistry and Physics, 17, 7605–7633, https://doi.org/10.5194/acp-17-7605-2017, 2017.

Guevara, M., Jorba, O., Tena, C., Denier van der Gon, H., Kuenen, J., Elguindi, N., Darras, S., Granier, C., and Pérez García-Pando, C.: Copernicus Atmosphere Monitoring Service TEMPOral Profiles (CAMS-TEMPO): Global and European Emission Temporal Profile Maps for Atmospheric Chemistry Modelling, Earth System Science Data, 13, 367–404, https://doi.org/10.5194/essd-13-367-2021, 2021.

https://doi.org/10.5194/egusphere-2025-1568
Preprint. Discussion started: 30 July 2025

Hall, J. V., Zibtsev, S. V., Giglio, L., Skakun, S., Myroniuk, V., Zhuravel, O., Goldammer, J. G., and Kussul, N.: Environmental and Political Implications of Underestimated Cropland Burning in Ukraine, Environmental research letters : ERL [Web site], 16, 064 019, https://doi.org/10.1088/1748-9326/abfc04, 2021.

Hansen, A. D. A., Rosen, H., and Novakov, T.: The Aethalometer — An Instrument for the Real-Time Measurement of Optical Absorption by Aerosol Particles, Science of The Total Environment, 36, 191–196, https://doi.org/10.1016/0048-9697(84)90265-1, 1984.

Hersbach, H., Bell, B., Berrisford, P., Hirahara, S., Horányi, A., Muñoz-Sabater, J., Nicolas, J., Peubey, C., Radu, R., Schepers, D., Simmons, A., Soci, C., Abdalla, S., Abellan, X., Balsamo, G., Bechtold, P., Biavati, G., Bidlot, J., Bonavita, M., De Chiara, G., Dahlgren, P., Dee, D., Diamantakis, M., Dragani, R., Flemming, J., Forbes, R., Fuentes, M., Geer, A., Haimberger, L., Healy, S., Hogan, R. J., Hólm, E., Janisková, M., Keeley, S., Laloyaux, P., Lopez, P., Lupu, C., Radnoti, G., de Rosnay, P., Rozum, I., Vamborg, F., Villaume, S., and Thépaut, J.-N.: The ERA5 Global Reanalysis, Quarterly Journal of the Royal Meteorological Society, 146, 1999–2049, https://doi.org/10.1002/qj.3803, 2020.

Hodnebrog, Ø., Myhre, G., and Samset, B. H.: How Shorter Black Carbon Lifetime Alters Its Climate Effect, Nature Communications, 5, 5065, https://doi.org/10.1038/ncomms6065, 2014.

Janssen, N. A., Gerlofs-Nijland, M. E., Lanki, T., Salonen, R. O., Cassee, F., Hoek, G., Fischer, P., Brunekreef, B., and Krzyzanowski, M.: Health Effects of Black Carbon, World Health Organization. Regional Office for Europe, ISBN 978-92-890-0265-3, 2012.

Jia, M., Evangeliou, N., Eckhardt, S., Huang, X., Gao, J., Ding, A., and Stohl, A.: Black Carbon Emission Reduction Due to COVID-19 Lockdown in China, Geophysical Research Letters, 48, e2021GL093 243, https://doi.org/10.1029/2021GL093243, 2021.

Koch, D., Schulz, M., Kinne, S., McNaughton, C., Spackman, J. R., Balkanski, Y., Bauer, S., Berntsen, T., Bond, T. C., Boucher, O., Chin, M., Clarke, A., De Luca, N., Dentener, F., Diehl, T., Dubovik, O., Easter, R., Fahey, D. W., Feichter, J., Fillmore, D., Freitag, S., Ghan, S., Ginoux, P., Gong, S., Horowitz, L., Iversen, T., Kirkev&aring, G, A., Klimont, Z., Kondo, Y., Krol, M., Liu, X., Miller, R., Montanaro, V., Moteki, N., Myhre, G., Penner, J. E., Perlwitz, J., Pitari, G., Reddy, S., Sahu, L., Sakamoto, H., Schuster, G., Schwarz, J. P., Seland, Ø., Stier, P., Takegawa, N., Takemura, T., Textor, C., van Aardenne, J. A., and Zhao, Y.: Evaluation of Black Carbon Estimations in Global Aerosol Models, Atmospheric Chemistry and Physics, 9, 9001–9026, https://doi.org/10.5194/acp-9-9001-2009, 2009.

Kuenen, J., Dellaert, S., Visschedijk, A., Jalkanen, J.-P., Super, I., and Denier van der Gon, H.: CAMS-REG-v4: A State-of-the-Art High-Resolution European Emission Inventory for Air Quality Modelling, Earth System Science Data, 14, 491–515, https://doi.org/10.5194/essd-14-491-2022, 2022.

Lack, D. A. and Langridge, J. M.: On the Attribution of Black and Brown Carbon Light Absorption Using the Ångström Exponent, Atmospheric Chemistry and Physics, 13, 10 535–10 543, https://doi.org/10.5194/acp-13-10535-2013, 2013.

Long, C. M., Nascarella, M. A., and Valberg, P. A.: Carbon Black vs. Black Carbon and Other Airborne Materials Containing Elemental Carbon: Physical and Chemical Distinctions, Environmental Pollution, 181, 271–286, https://doi.org/10.1016/j.envpol.2013.06.009, 2013.

Mao, Y., Li, Q., Chen, D., Zhang, L., Hao, W.-M., and Liou, K.-N.: Top-down Estimates of Biomass Burning Emissions of Black Carbon in the Western United States, Atmospheric Chemistry and Physics, 14, https://doi.org/10.5194/acp-14-7195-2014, 2014.

Meirink, J. F., Bergamaschi, P., and Krol, M. C.: Four-Dimensional Variational Data Assimilation for Inverse Modelling of Atmospheric Methane Emissions: Method and Comparison with Synthesis Inversion, Atmospheric Chemistry and Physics, 8, 6341–6353, https://doi.org/10.5194/acp-8-6341-2008, 2008.

Michalak, A. M., Randazzo, N. A., and Chevallier, F.: Diagnostic Methods for Atmospheric Inversions of Long-Lived Greenhouse Gases, Atmospheric Chemistry and Physics, 17, 7405–7421, https://doi.org/10.5194/acp-17-7405-2017, 2017.

https://doi.org/10.5194/egusphere-2025-1568
Preprint. Discussion started: 30 July 2025

Monteil, G. and Scholze, M.: Regional CO_2 Inversions with LUMIA, the Lund University Modular Inversion Algorithm, v1.0, Geoscientific Model Development, 14, 3383–3406, https://doi.org/10.5194/gmd-14-3383-2021, 2021.

Müller, T. and Fiebig, M.: ACTRIS In Situ Aerosol: Guidelines for Manual QC of AE33 Absorption Photometer Data, 2021.

Munassar, S., Monteil, G., Scholze, M., Karstens, U., Rödenbeck, C., Koch, F.-T., Totsche, K. U., and Gerbig, C.: Why Do Inverse Models Disagree? A Case Study with Two European CO_2 Inversions, Atmospheric Chemistry and Physics, 23, 2813–2828, https://doi.org/10.5194/acp-23-2813-2023, 2023.

Ogren, J. A., Wendell, J., Andrews, E., and Sheridan, P. J.: Continuous Light Absorption Photometer for Long-Term Studies, Atmospheric Measurement Techniques, 10, 4805–4818, https://doi.org/10.5194/amt-10-4805-2017, 2017.

Park, R. J., Jacob, D. J., Palmer, P. I., Clarke, A. D., Weber, R. J., Zondlo, M. A., Eisele, F. L., Bandy, A. R., Thornton, D. C., Sachse, G. W., and Bond, T. C.: Export Efficiency of Black Carbon Aerosol in Continental Outflow: Global Implications, Journal of Geophysical Research: Atmospheres, 110, https://doi.org/10.1029/2004JD005432, 2005.

Petzold, A. and Schönlinner, M.: Multi-Angle Absorption Photometry—a New Method for the Measurement of Aerosol Light Absorption and Atmospheric Black Carbon, Journal of Aerosol Science, 35, 421–441, https://doi.org/10.1016/j.jaerosci.2003.09.005, 2004.

Petzold, A., Ogren, J. A., Fiebig, M., Laj, P., Li, S.-M., Baltensperger, U., Holzer-Popp, T., Kinne, S., Pappalardo, G., Sugimoto, N., Wehrli, C., Wiedensohler, A., and Zhang, X.-Y.: Recommendations for Reporting "Black Carbon" Measurements, Atmospheric Chemistry and Physics, 13, 8365–8379, https://doi.org/10.5194/acp-13-8365-2013, 2013.

Pisso, I., Sollum, E., Grythe, H., Kristiansen, N. I., Cassiani, M., Eckhardt, S., Arnold, D., Morton, D., Thompson, R. L., Groot Zwaaftink, C. D., Evangeliou, N., Sodemann, H., Haimberger, L., Henne, S., Brunner, D., Burkhart, J. F., Fouilloux, A., Brioude, J., Philipp, A., Seibert, P., and Stohl, A.: The Lagrangian Particle Dispersion Model FLEXPART Version 10.4, Geoscientific Model Development, 12, 4955–4997, https://doi.org/10.5194/gmd-12-4955-2019, 2019.

Seibert, P. and Frank, A.: Source-Receptor Matrix Calculation with a Lagrangian Particle Dispersion Model in Backward Mode, Atmospheric Chemistry and Physics, 4, 51–63, https://doi.org/10.5194/acp-4-51-2004, 2004.

Sinha, P. R., Kondo, Y., Koike, M., Ogren, J. A., Jefferson, A., Barrett, T. E., Sheesley, R. J., Ohata, S., Moteki, N., Coe, H., Liu, D., Irwin, M., Tunved, P., Quinn, P. K., and Zhao, Y.: Evaluation of Ground-Based Black Carbon Measurements by Filter-Based Photometers at Two Arctic Sites, Journal of Geophysical Research: Atmospheres, 122, 3544–3572, https://doi.org/10.1002/2016JD025843, 2017.

Soulie, A., Granier, C., Darras, S., Zilbermann, N., Doumbia, T., Guevara, M., Jalkanen, J.-P., Keita, S., Liousse, C., Crippa, M., Guizzardi, D., Hoesly, R., and Smith, S. J.: Global Anthropogenic Emissions (CAMS-GLOB-ANT) for the Copernicus Atmosphere Monitoring Service Simulations of Air Quality Forecasts and Reanalyses, Earth System Science Data, 16, 2261–2279, https://doi.org/10.5194/essd-16-2261-2024, 2024.

Stohl, A., Klimont, Z., Eckhardt, S., Kupiainen, K., Shevchenko, V. P., Kopeikin, V. M., and Novigatsky, A. N.: Black Carbon in the Arctic: The Underestimated Role of Gas Flaring and Residential Combustion Emissions, Atmospheric Chemistry and Physics, 13, 8833–8855, https://doi.org/10.5194/acp-13-8833-2013, 2013.

Textor, C., Schulz, M., Guibert, S., Kinne, S., Balkanski, Y., Bauer, S., Berntsen, T., Berglen, T., Boucher, O., Chin, M., Dentener, F., Diehl, T., Easter, R., Feichter, H., Fillmore, D., Ghan, S., Ginoux, P., Gong, S., Grini, A., Hendricks, J., Horowitz, L., Huang, P., Isaksen, I., Iversen, I., Kloster, S., Koch, D., Kirkevåg, A., Kristjansson, J. E., Krol, M., Lauer, A., Lamarque, J. F., Liu, X., Montanaro, V., Myhre, G., Penner, J., Pitari, G., Reddy, S., Seland, Ø., Stier, P., Takemura, T., and Tie, X.: Analysis and Quantification of the Diversities of Aerosol Life Cycles within AeroCom, Atmospheric Chemistry and Physics, 6, 1777–1813, https://doi.org/10.5194/acp-6-1777-2006, 2006.

https://doi.org/10.5194/egusphere-2025-1568
Preprint. Discussion started: 30 July 2025

Thornhill, G. D., Collins, W. J., Kramer, R. J., Olivié, D., Skeie, R. B., O'Connor, F. M., Abraham, N. L., Checa-Garcia, R., Bauer, S. E., Deushi, M., Emmons, L. K., Forster, P. M., Horowitz, L. W., Johnson, B., Keeble, J., Lamarque, J.-F., Michou, M., Mills, M. J., Mulcahy, J. P., Myhre, G., Nabat, P., Naik, V., Oshima, N., Schulz, M., Smith, C. J., Takemura, T., Tilmes, S., Wu, T., Zeng, G., and Zhang, J.: Effective Radiative Forcing from Emissions of Reactive Gases and Aerosols – a Multi-Model Comparison, Atmospheric Chemistry and Physics, 21, 853–874, https://doi.org/10.5194/acp-21-853-2021, 2021.

Tsikerdekis, A., Hasekamp, O. P., Schutgens, N. A. J., and Zhong, Q.: Assimilation of POLDER Observations to Estimate Aerosol Emissions, Atmospheric Chemistry and Physics, 23, 9495–9524, https://doi.org/10.5194/acp-23-9495-2023, 2023.

Ullrich, B., Wankmüller, R., and Schindlbacher, S.: Inventory Review 2023, Tech. Rep. 4, Centre on Emission Inventories and Projections, 2023.

van der Werf, G. R., Randerson, J. T., Giglio, L., van Leeuwen, T. T., Chen, Y., Rogers, B. M., Mu, M., van Marle, M. J. E., Morton, D. C., Collatz, G. J., Yokelson, R. J., and Kasibhatla, P. S.: Global Fire Emissions Estimates during 1997–2016, Earth System Science Data, 9, 697–720, https://doi.org/10.5194/essd-9-697-2017, 2017.

Wang, P., Wang, H., Wang, Y. Q., Zhang, X. Y., Gong, S. L., Xue, M., Zhou, C. H., Liu, H. L., An, X. Q., Niu, T., and Cheng, Y. L.: Inverse Modeling of Black Carbon Emissions over China Using Ensemble Data Assimilation, Atmospheric Chemistry and Physics, 16, 989–1002, https://doi.org/10.5194/acp-16-989-2016, 2016.

Wang, X., Wang, Y., Hao, J., Kondo, Y., Irwin, M., Munger, J. W., and Zhao, Y.: Top-down Estimate of China's Black Carbon Emissions Using Surface Observations: Sensitivity to Observation Representativeness and Transport Model Error, Journal of Geophysical Research - Atmospheres, 118, 5781–5795, https://doi.org/10.1002/jgrd.50397, 2013.

Zanatta, M., Gysel, M., Bukowiecki, N., Müller, T., Weingartner, E., Areskoug, H., Fiebig, M., Yttri, K. E., Mihalopoulos, N., Kouvarakis, G., Beddows, D., Harrison, R. M., Cavalli, F., Putaud, J. P., Spindler, G., Wiedensohler, A., Alastuey, A., Pandolfi, M., Sellegri, K., Swietlicki, E., Jaffrezo, J. L., Baltensperger, U., and Laj, P.: A European Aerosol Phenomenology-5: Climatology of Black Carbon Optical Properties at 9 Regional Background Sites across Europe, Atmospheric Environment, 145, 346–364, https://doi.org/10.1016/j.atmosenv.2016.09.035, 2016.

Zhang, L., Henze, D. K., Grell, G. A., Carmichael, G. R., Bousserez, N., Zhang, Q., Torres, O., Ahn, C., Lu, Z., Cao, J., and Mao, Y.: Constraining Black Carbon Aerosol over Asia Using OMI Aerosol Absorption Optical Depth and the Adjoint of GEOS-Chem, Atmospheric Chemistry and Physics, 15, 10 281–10 308, https://doi.org/10.5194/acp-15-10281-2015, 2015.

Zhao, X., Zhao, Y., Chen, D., Li, C., and Zhang, J.: Top-down Estimate of Black Carbon Emissions for City Clusters Using Ground Observations: A Case Study in Southern Jiangsu, China, Atmospheric Chemistry and Physics, 19, 2095–2113, https://doi.org/10.5194/acp-19-2095-2019, 2019.

Zotter, P., Herich, H., Gysel, M., El-Haddad, I., Zhang, Y., Močnik, G., Hüglin, C., Baltensperger, U., Szidat, S., and Prévôt, A. S. H.: Evaluation of the Absorption Ångström Exponents for Traffic and Wood Burning in the Aethalometer-based Source Apportionment Using Radiocarbon Measurements of Ambient Aerosol, Atmospheric Chemistry and Physics, 17, 4229–4249, https://doi.org/10.5194/acp-17-4229-2017, 2017.